Shape Effect of Rockfall Impacting Sandy Soil Cushion Layer–Reinforced Concrete Slab Composite Structure

Xuefeng MEI [1], Teng WANG [1], Tian SU [2, 3] *, Dong ZHU [4], Bangxiang LI [2], Jianli WU [5]

[1] *School of Architecture and Engineering, Weifang University of Science and Technology, Weifang, Shandong, China, 262700*
[2] *School of Civil and Architectural Engineering, Shandong University of Technology, Zibo, Shandong, China, 255000*
[3] *Department of Engineering and Management, International College, Krirk University, Anusaowaree, Bangkhen, Bangkok 10220, Thailand*
[4] *The 3rd Geological Brigade of Zhejiang Province, Jinhua, Zhejiang, China, 321000*
[5] *College of Civil Engineering and Architecture, Zhejiang University of Water Resources and Electric Power, Hangzhou, Zhejiang, China, 310018*

http://doi.org/10.5755/j02.ms.36216

Received 30 January 2024; accepted 18 March 2024

The impact effects of falling rocks on sand–reinforced concrete slab composite protective structures involve several factors. Among them, the existing codes are unable to consider the effect of rockfall shape and the angle of contact between the rockfall and the object on the impact force as well as the depth of penetration. Based on extensive field investigation, this paper proposes a shape factor to simplify the rockfall into an ellipsoid and determines the shape and dimensions of the rockfall by three-dimensional axis length. Besides, a coupled SPH-FEM numerical calculation model is established and validated through comparison with a large-scale outdoor test of a rockfall impact protection structure. Finally, the effects of rockfall shape and impact angle on the symbolic parameters including impact force, impulse and energy in the impact process are revealed. The findings indicate that the maximum force and displacement of the midpoint of the bottom of the reinforced concrete slab have relative errors within 5.0 % when compared to the model test, confirming the precision of the models discussed in this paper. For the same rockfall, the peak force decreases with the impact angle increasing; taking the same volume of spherical rockfall as the reference, under the same rockfall pattern, the peak impact force and impulse amplification factor decreases with the increase in contact attitude angle. Additionally, the scaling effect becomes more pronounced when the shape factor of the rockfall is smaller; under the same shape factor, the impact depth of the cushion layer is the smallest when the attitude angle is 45°, and the maximum when the impact angle is 90°; the SPH-FEM coupling algorithm could reasonably reproduce the pit-forming process of sand and soil, and it is very effective in simulating the flow effect of soil particles under impact.

Keywords: rockfall, shape factor, impact response, SPH-FEM coupling method.

1. INTRODUCTION

Rockfall is a typical mountain disaster, with high-energy, sudden and random characteristics [1 – 4]. To mitigate the great hazards of rockfalls in the project impact area, active and passive protection structures can be used for management. Usually, active protection methods include active nets [5, 6], anchoring [7], and targeted blasting [8]. Passive protection includes passive nets [9 – 11], rock sheds [12 – 16], and barriers [17 – 20]. The choice of protection structure depends on the topography and geomorphology of the defense area, construction conditions, and the kinetic characteristic parameters of rockfalls. Among them, the impact force of rockfalls is the main factor that determines the type and cross–section size of the protective structure. To prevent the maximal impact force of rockfalls from surpassing the ultimate design capacity of the protective measure, accurate evaluation and prediction of the impact effect of rockfall is a prerequisite for effective protection design [21, 22].

The shape of rockfall under natural conditions is characterized by irregularity and randomness, which in turn leads to many factors influencing the impact force of rockfall including mass, velocity, shape, and impact angle. Among them, the influence of rockfall weight and impact velocity are the main areas of concern. However, the impact effect is affected by the impact angle and rockfall shape, which is often neglected. In many impact tests, most of the researchers and the current codes simplify the rockfall shape, such as sphere [23], cube [24, 25], or cylinder [26]. Among a series of rockfall shape assumptions, the spherical rockfall cannot consider how the impact angle influences the impact process; if rockfall is regarded as a spherical projectile, they cannot effectively consider the shape of the impacting end and the randomness with respect to the impact angle; therefore, the results obtained are not generalizable. In practical engineering, the design of protective structures using the calculation model of rockfall impact force obtained with specific assumptions may be an important reason for the damage to the constructed structures [27] (Fig. 1).

*Corresponding author. Tel.: +86-19953368540.
E-mail: *sutian@sdut.edu.cn* (T. Su)

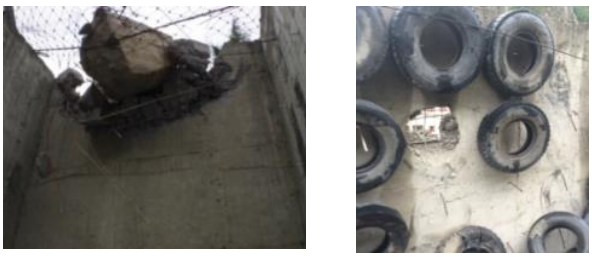

a b

Fig. 1. Disaster caused by rockfall: a – RC-slab damage cases; b – retaining wall damage cases

Typically, impact tests, theoretical analyses, and numerical simulations are the primary research techniques employed to investigate how rockfall shape affects the impact response. Perera et al. [28] and Huang et al. [29] demonstrated the form of rockfall is important in determining the impact force, but there are no quantitative conclusions to demonstrate which shape of rockfall causes a greater force. Yan et al. [30] investigated the force and depth of impact caused by three common types of rockfalls impacting a cushion layer, namely spherical, conical, and flat head, based on impact test and dimensionless theory. However, this method can only consider the impact response under the fixed impact pattern. Pichler et al. [31] studied the characteristic values of impact depth and impact force generated by a 20 t cubic rockfall impacting layers of gravel. This information can serve as a guide for designing gravel dissipation layers for rockfalls. In addition, the dynamic response of a 9 t cubic rockfall impacting a reinforced embankment was investigated by Peila et al. [32].

Limited by experimental conditions, theoretical analysis and numerical simulation have become important tools in the current research. Yang and Zhou [33] established a new model for calculating the force of rockfall in an elliptical trajectory, but the model did not consider how the impact force is affected by the impact angle. Wang and Cavers [34] deduced the calculation method of maximum force and penetration depth of cubic rockfall through geotechnics. Dattola et al. [35] demonstrated through visco–elastic plasticity theory that prismatic rockfalls have a greater maximum depth of penetration and impact force than spherical rockfalls. Prisco and Vecchiotti [36] established a vis–coplasticity model based on spherical rockfalls and gave a method for calculating the force of rockfalls. With the rapid development of computers, numerical calculations have achieved wide application in civil engineering. Among them, most of the research regarding the influence of rockfall shape on impact effect uses the finite element method [37 – 40]. Although the finite element method is very effective in solving static problems, it is difficult to guarantee computational accuracy and convergence for the simulation of large deformation materials. Granular materials such as sand and gravel soil are usually used as energy dissipation layers in rockfall protection projects. When the rockfall contacts with the granular layer of the cushion layer, the rigid cushion layer hardly shows obvious flow and large deformation characteristics, and the use of the finite element method may lead to mesh distortion and computational failure [41]. In contrast to the finite element method, studies on the impact effect of rockfall using the discrete element method have also been reported [42]. Although the discrete element method can consider the crushing characteristics of rockfall during the impact process, most studies didn't consider how the shape and pose of rockfalls influence the outcome of impact, and the parameter calibration is very complicated [43].

As described above, the typical equations used to determine the impact force of rockfall are derived from a head–on the impact between spherical rockfall and the object. There is limited research on how the shape and impact manner of rockfall influences impact response, with experimental analysis being underutilized. What's more, experimental analyses cannot effectively consider the shape of the impact end and the randomness of the impact angle. In addition, the theoretical analysis has too many qualifications and is less applicable. Smoothed Particle Hydrodynamics (SPH) belongs to a pure Lagrangian meshless particle method used to calculate the mechanics of a continuous medium. Since there is no mesh relationship between the elements, it is well suited for modeling granular substances like sand and soil. Nevertheless, the computational efficiency of using a single SPH method is relatively low. For a protective structure made of reinforced concrete and sand layers, the use of SPH particles in the bedding region and finite element meshes in other small deformation areas can ensure computational efficiency and accuracy [44 – 45].

In this paper, firstly, through the statistical and observation results of the morphology of rockfall in the field, the shape factor was introduced to describe the size and morphology of rockfall. Then the numerical model using SPH-FEM coupling method is constructed and compared with the outdoor large–scale rockfall impact test data, which validates the coupling algorithm. Ultimately, considering the effect of the shape factor of rockfall and impact angle, the impact response is further investigated.

2. CALCULATION METHOD

2.1. SPH methodology

SPH is first applied to fluid calculations. Since there is no mesh in the computation, large mesh deformation does not exist. In this approach, the computational area is divided into a series of individual particles that are connected by a kernel function (Fig. 2). The particle's field variables are determined by integrating the functions:

$$\langle f(x)\rangle = \int_{\Omega} f(x')W\left(x-x', h\right)dx' . \tag{1}$$

The continuous integral in Eq. 1 can be transformed into a discrete summation equation:

$$\langle f(x)\rangle = \sum_{j=1}^{N} \frac{m_j}{\rho_j} f\left(x_j\right)W\left(x-x_j, h\right), \tag{2}$$

where j represents the number of particles; m_j is the mass of the particles; ρ_j is the density of the particles.

Smooth kernel functions need to satisfy three basic conditions:

a) normalization conditions, i.e., integrating to 1 in its region of integration:

$$\int_{\Omega} W(x-x')dx' = 1. \tag{3}$$

b) the Dirac Delta function is satisfied when the smooth length h tends to zero:

$$\lim_{h\to 0} = W(x-x') = \delta(x-x'). \tag{4}$$

c) the smooth kernel function must satisfy the tightness condition.

$$W(x-x') = 0. \tag{5}$$

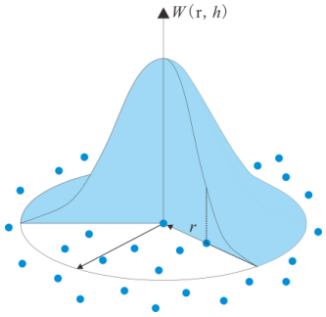

Fig. 2. Kernel function

2.2. SPH–FEM coupling theory

The coupling algorithm can generally be divided into two types, i.e. fixed coupling algorithm and adaptive coupling algorithm. The former fixes the SPH calculation and the FEM area in the whole calculation process, and the latter applies the FEM method in the initial calculation phase, and transforms the deformed regions into SPH particles according to the customized conditions in the calculation process.

In this algorithm, the contact conditions in the Runge–Kutta method are typically used to effectively facilitate the coupling between the finite element interface and the smooth particles:

$$\begin{cases} g \leqslant 0 \\ g \cdot t = 0 \\ t \geqslant 0 \end{cases}, \tag{6}$$

where g and t refer to the gap function and contact force, respectively.

During the coupling calculation, the particles and elements are respectively defined as slave nodes and master surfaces (Fig. 3). A detailed guide on how to apply the suggested model is available in the flowchart shown in Fig. 4.

In addition, according to the material constitutive model, the stress and strain rate are determined. Subsequently, the forces acting on the elements' nodes and the SPH particles, as well as adjacent nodes, are identified. This process is repeated through iterations to find solutions for the entire computation time. In this paper, the cushion layer with large deformation is defined as SPH particles, while the reinforced concrete slab with small deformation and the rockfall are defined as finite element. The impact between the rockfall and the cushion layer can be interpreted as a normal "spring" at the interface of mutual contact, and if the intruding node penetrates the permeable surface, it will be subject to the reaction force of the spring.

The system of coupled equations is computed using the stable frog jump explicit integration method, which needs to satisfy the following equations:

$$\begin{cases} \Delta t_{SPH-FEM} = \min\left\{\Delta t_{SPH}, \Delta t_{FEM}\right\} \\ \Delta t_{SPH} = \alpha \dfrac{h}{c} \\ \Delta t_{SPH} \leq \Delta t_{cr} = \dfrac{l}{c} \end{cases}, \tag{7}$$

where L is the minimum cell size; C is the material sound velocity; α is the time step scaling factor.

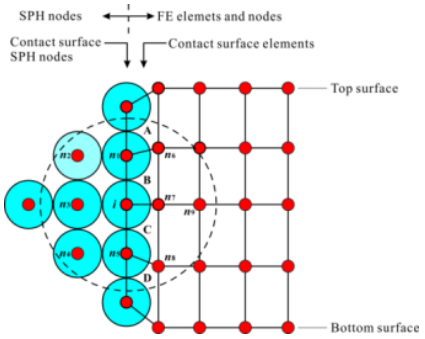

Fig. 3. SPH-FEM interface coupling mode

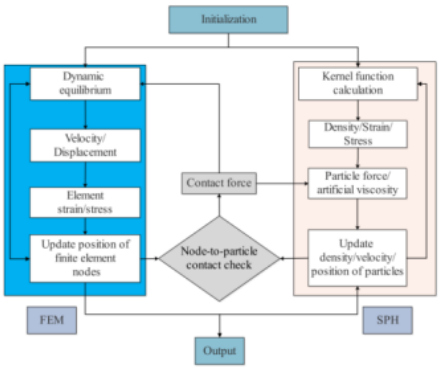

Fig. 4. Solution procedure for SPH-FEM contact algorithm

3. RESEARCH METHODOLOGY AND CONTENT

3.1. Field survey and analysis

Rockfall is controlled by the nature of the rockfall mass and the structural surface. And the random variation in the shape under natural conditions is very significant, in which the collision of rockfall with the ground and the protective structure may occur in the form of face-to-face contact, point-to-face contact, and prismatic-to-face contact, and other random forms. Different collision modes will affect the effects such as rockfall impact force and impact depth.

The 2017 Sichuan Kangding Jiuzhaigou earthquake induced a large number of high level collapse rockfalls (Fig. 5). According to the field investigation, the rockfall shape has a large variability, with significant differences compared to a simplified sphere. Therefore, an ellipsoid is used to approximate and simplify the rockfall in this paper.

The dimension of a rockfall in three axes, and shape factor were introduced to describe the irregularity of the rockfalls. The shape factor ψ is defined as:

$$\psi = \frac{\sqrt{bc}}{a}, \tag{8}$$

where a is the long axis of the ellipsoidal rockfall; b is the longest of all the secant lines perpendicular to a; c is the longest secant line perpendicular to both a and b. When the lengths of the three axes are the same, i.e. when ψ = 1.0, the rockfall is simplified to a sphere.

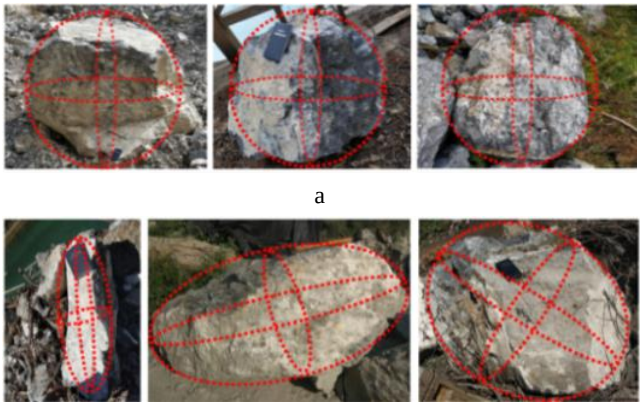

a

b

Fig. 5. Typical shapes of rockfalls: a – spherical; b – ellipsoid

3.2. Outdoor rockfall impact experiment

An outdoor large–scale test platform was constructed (Fig. 6 a). The dimension of the reinforced concrete slab is displayed in Fig. 6 b.

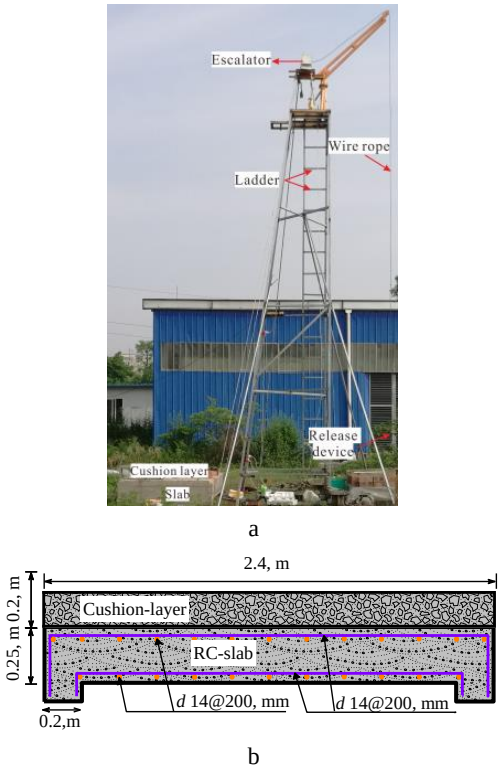

a

b

Fig. 6. Test platform: a – test equipment; b – cushion layer

The concrete slab's bars are set orthogonally and vertically. All reinforcement bars are 14 mm in diameter and spaced 200 mm. The rockfall was made by filling concrete in a spherical steel mold with a mass of 70.7 kg. Indoor geotechnical tests were conducted on the cushion layer soil, and the general density of soil particles in the cushion layer was 1540 kg/m^3 with a water content of 5.4 %. According to the grading curve (Fig. 7), the average particle size D_{50} = 0.1 mm.

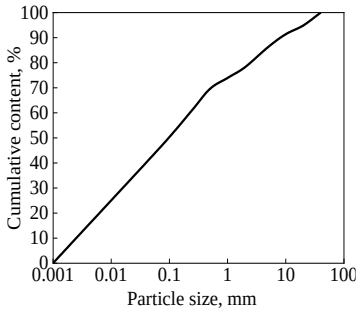

Fig. 7. Soil particle grading curve

4. NUMERICAL SIMULATION VALIDATION OF MODEL TESTS

To confirm the rationality of the SPH–FEM coupling algorithm, a numerical model was established in this paper (Fig. 8). In the computational model, except for the cushion layer which is an SPH particle, the rest of the parts use finite elements. In addition, since the deformation of the rockfall during the impact is not considered, the block is assumed to be a rigid body in the numerical simulation.

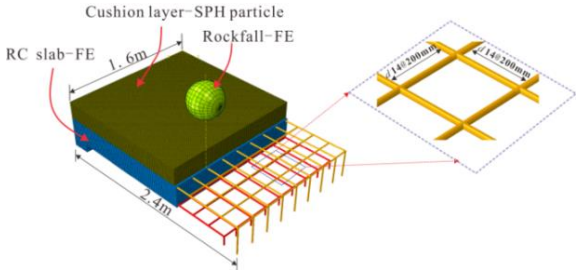

Fig. 8. SPH-FEM numerical model

4.1. Material parameters

In this work, the Drucker-Prager constitutive model was used to define the soil material. In addition, the reinforcing was modeled with a three-line model, which can well simulate the strain rate effect of the material:

$$\sigma = \begin{cases} E \cdot \varepsilon & \varepsilon \leqslant \varepsilon_0 \\ \sigma_0 & \varepsilon_0 < \varepsilon \leqslant \varepsilon_{0,h} \\ \sigma_0 + E_t \cdot (\varepsilon - \varepsilon_{0,h}) & \varepsilon > \varepsilon_{0,h} \end{cases}, \tag{9}$$

where E represents the elastic modulus of the steel; $\varepsilon_{0,h}$ denotes the initial strain during the strengthening phase; ε_0 is the yield strain.

To analyze the entire damage process of concrete stiffness under dynamic loading, concrete is simulated using the Concrete Damaged Plasticity (CDP) model [46], and the damage of concrete stiffness can be defined as:

$$E = (1-d)E_0, \quad (10)$$

where E_0 is the initial elastic modulus of nondestructive; d is the damage factor.

The concrete's damage factor can be determined using the Simpson Integration Method [47], and the main parameters required for the calculations in this paper are given in Table 1.

4.2. Contact setting and boundary condition

The model's boundary condition is to constrain the degrees of freedom of the bottom support in 3 directions. The contact relationship between different material components is defined using a penalty function, where the friction coefficient of the block–cushion layer is 0.4, and the cushion layer-reinforced concrete slab friction coefficient is 0.48, respectively. Besides, the interaction between reinforcement and concrete is simulated by embedding. To save computational costs, the falling height of the block is converted into an impact velocity directed toward the center of mass of the rockfall.

4.3. Comparative validation results

The comparison of the displacement and acceleration duration curves at the center of the reinforced concrete slab obtained from a computer simulation and the actual test results is shown in Fig. 9.

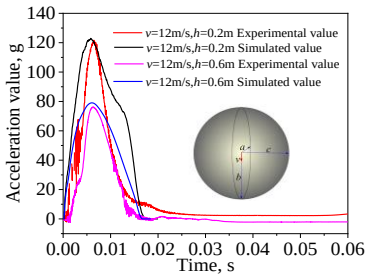

a

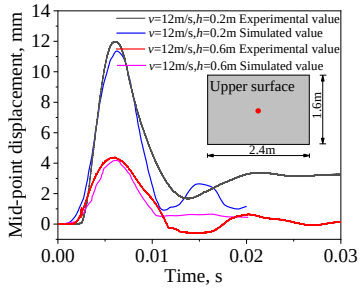

b

Fig. 9. Experimental and numerical results: a – impact force; b – displacement of concrete slab

The rockfall mass considered is 70.7 kg, with cushion layer thicknesses of 0.2 m and 0.6 m, respectively. The results show that the relative error between the test values and the numerical simulations is small. According to the acceleration duration curves, we can see that the rockfall impact process obtained from the actual measurement and simulation lasted about 10 ms, in which the loading compression and unloading rebound time each accounted for half of the total time. For cushion layer thicknesses of 0.2 m and 0.6 m, the impact velocity is 12 m/s, and the maximum values of measured and simulated acceleration are 121.7 g and 123 g, 76.2 g and 79.0 g, with a relative error of 1.1 % and 3.7 %, respectively (Fig. 9 a).

The maximum acceleration decreases with the cushion layer thickness increasing under the same conditions, and many scholars have given similar proof conclusions for this change characteristic of the force [48]. For the displacement of the midpoint of the reinforced concrete slab (Fig. 9 b), the corresponding errors between the measured and simulated values of the slab center displacement are within 5.0 % for the same impact velocity and cushion layer thicknesses. The above analysis proves that the coupled SPH-FEM method of simulation used in this paper is reasonable.

5. NUMERICAL SIMULATION OF ROCKFALL IMPACT PROTECTION STRUCTURE

According to the validated SPH-FEM coupled numerical simulation method, the effect of rockfall impact protection structure including the influence of rockfall shape was investigated. Initially, the study outlines the calculation parameters involving various shape factors and impact angles. Subsequently, it computes the impact force and process of rockfall for different shape factors. Lastly, it examines the impact effect's dependence on the shape factor and impact angle.

5.1. SPH-FEM modeling

The reinforced concrete slab size and reinforcement used in the numerical model are the same as that in the previous tests. In the simulation, SPH particle is used for the cushion layer components and FE elements for the other components. The cushion layer thickness and loading speed were kept constant at 0.2 m and 10 m/s, respectively. The computational model can be seen in Fig. 10, and the material failure criterion, calculation parameters and boundary conditions are consistent with the preceding paragraph.

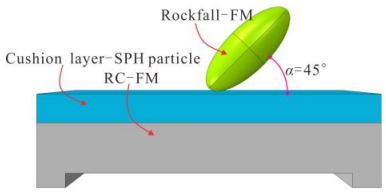

Fig. 10. Numerical model of rockfall impact protection structure

Table 1. Material parameters

Material type	Density, kN·m^{-3}	Elastic modulus, MPa	Poisson's ratio	Shear expansion angle, °	Eccentricity	f_{b0}/f_{c0}
Concrete	25.0	30000	0.21	38	0.10	1.16
Cushion layer	15.4	34.0	0.28	Friction angle, °	Yield strength, kPa	Shear expansion angle, °
				26	200.0	0.0
Rebar	78.0	200000	0.27	Yield strength, MPa	Ultimate strength, MPa	Extreme tensile strain
				502	662.3	0.130

5.2. Calculation cases

In this study, impact conditions of rockfalls with different shape factors and impact angles are designed, as shown in Table 2. Considering the randomness of the impact angle of rockfalls in the impact process, three impact angles of 0°, 45° and 90° were designed. To make the calculation easier, it is assumed that b=c in the calculation.

5.3. Results and analysis

5.3.1. Influence of shape effects on forces

Fig. 11 shows the effect on the duration curves of impact force for different shape factors and impact angles. The results show that, when other conditions are the same, the shape factor and impact angles are significant in determining the peak force. When the shape factors are equal, the greater the impact angle, the shorter the contact time and the higher the impact force. Taking the spherical rockfall (ψ = 1) as the base, the ratio of the force (F) of the rockfall with any shape factor to the force (F_0) of the spherical rockfall is defined as the amplification factor of the impact force:

$$\lambda_F=F/F_0, \quad (11)$$

where λ_F is the impact amplification factor; F is the peak impact force, N; F_0 is the peak impact force, N of the spherical rockfall (ψ = 1).

Similarly, the impulse amplification factor λ_I is defined as:

$$\lambda_I=I/I_0, \quad (12)$$

where λ_I is the impulse amplification factor; I is the peak impulse, N·S of rockfall for other conditions; I_0 is the peak impulse, N·S simplified to spherical rockfall (ψ = 1).

Fig. 12 shows the effect of the shape factor and impact angle of rockfall on force and impulse. The results show that when a shape factor is 0.4 and the impact angle is 0° and 90°, the maximum force of the ellipsoidal rockfall is magnified by 1.42 times and 0.46 times than that of the spherical rockfall in the same case. As the shape factor of the rockfall increases, the force is less affected by the impact angle. In addition, the effect of the shape factor and impact angle on the impulse follows the same pattern as that of the impact force, but the degree of influence is significantly weaker. At a shape factor of 0.40 and impact angle of 0°, 45° and 90°, the impulse amplification factors are 1.0, 0.81, and 0.77, respectively; if the shape factor rises to 0.79, the impulse amplification factors at the three impact angles are 1.0, 0.96 and 0.95, respectively. Thus the variation range of the force induced by the randomness of the rockfall shape and the impact angle is very large. In practical engineering, the simplified method of rockfall neglecting the shape and pose is misguiding.

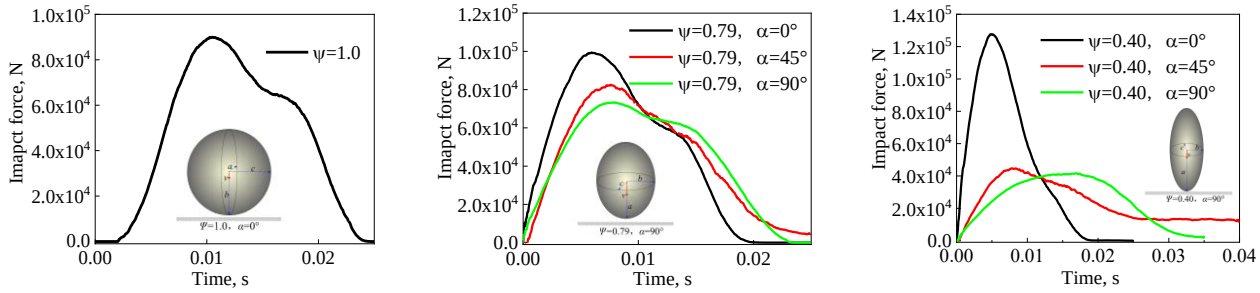

Fig. 11. Impact forces: a – ψ = 1.0; b – ψ = 0.79; c – ψ = 0.40

Table 2. Calculation conditions

Impact velocity, m/s	Length, m	ψ = 0.40		ψ = 0.79		ψ = 1.0	
10	*a*	0.44	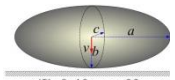	0.28	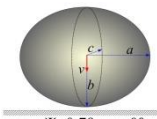	0.24	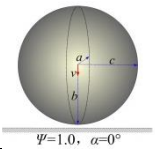
	b	0.177	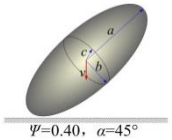	0.222	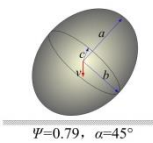	0.24	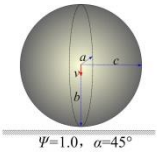
	c	0.177	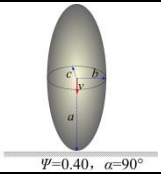	0.222	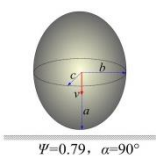	0.24	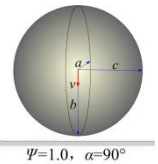

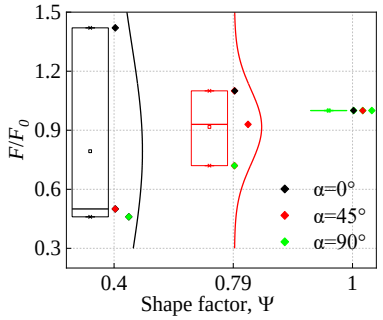

a

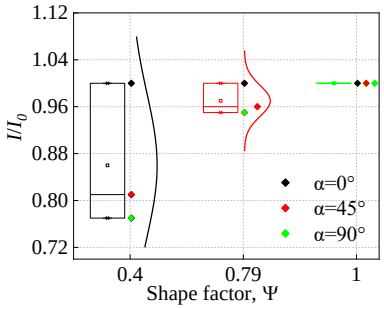

b

Fig. 12. Impact and impulse effects: a – force; b – impulse

5.3.2. Effect of rockfall shape on energy

The primary purpose of the cushion layer is to absorb the rockfall's kinetic energy by undertaking significant deformations, thereby preventing the structure from sustaining rigid and brittle damage. Fig. 13 summarizes how the energy dissipation pattern is influenced by the shape factor and impact angle.

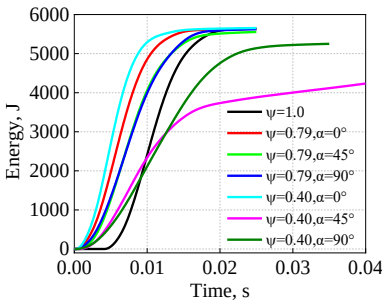

Fig. 13. Duration curve of inelastic strain energy of cushion layer

The findings introduce that the trend of plastic deformation energy change in the cushion layer is consistent for different shapes and impact angles of rockfalls in the impact process. But because of the shape factor of 0.40, the maximum impact force generated at the impact angles of 45° and 90° is less than that of the maximum impact force at the impact angle of 0°(Fig. 13). Therefore, the plastic deformation energy generated by the impact conditions with impact angles of 45° and 90° is significantly larger than that at 0°.

To prevent rockfalls from penetrating through the cushion layer and directly touching the rigid concrete structure, the impact depth of the rockfall is one of the crucial factors in designing protective structures, which largely influences the minimum thickness needed for the cushion layer. Fig. 14 shows the effect of the rockfall shape factor and impact angle on the maximum impact depth of the cushion layer.

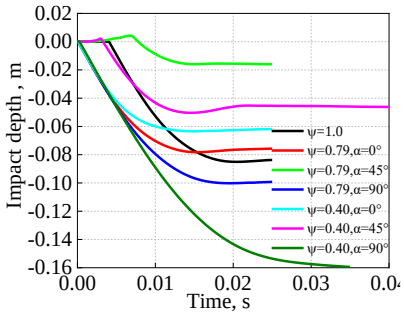

Fig. 14. Duration curve of impact depth

The findings indicate that when the rockfall has the same mass and velocity, it can produce a deformation of the cushion layer ranging from between 1.8 cm and 16 cm. In addition, for the same rockfall, the impact angle that resulted in the deepest impact was 90°, while the shallowest impact occurred at an impact angle of 45°. Therefore, the range of variation in maximum impact depth due to the randomness of rockfall shape and impact angle is too large to be ignored.

Fig. 15 shows the stress of the cushion layer at different moments when the shape factor of the rockfall is 0.40 and the impact angle is 45°, respectively. With the increase in impact time, the soil particles in the cushion layer are compressed, and the Mises stress increases, and the maximum stress increases from 0 to 1.5 × 10^6 Pa throughout the impact process. The cushion layer experienced a significant plastic deformation of 4.2 cm in the end, as shown in Fig. 14, indicating substantial soil deformation during the impact. Different from spherical rockfall, the ellipsoidal rockfall will generate a larger rotation in the whole impact process because the impact velocity and the ellipsoidal axis of symmetry is not in the same straight line, and the ultimate collision pose and the initial pose show a significant difference.

According to the displacement cloud diagram of the cushion layer (Fig. 16), the greatest compression deformation occurs in the region where the rockfall directly contacts the soil.

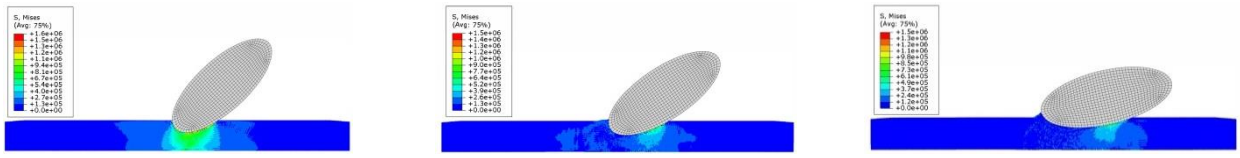

a b c

Fig. 15. Stresses at different moments in the cushion layer (ψ = 0.40, α = 45°): a – 10 ms; b – 30 s; c – 40 ms

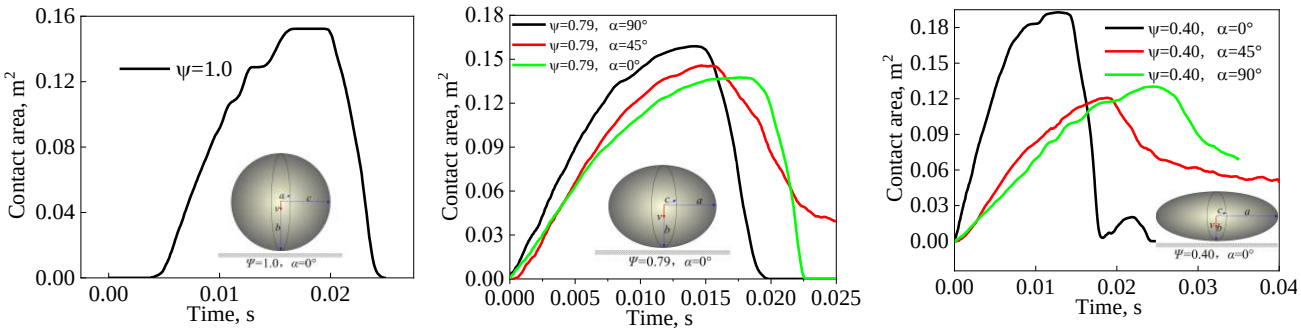

Fig. 17. Impact forces: a – ψ = 1.0; b – ψ = 0.79; c – ψ = 0.40

The soil particles experience significant flow effects as they are extruded by the rockfall. Therefore, it is very scientific for the simulation of granular materials using the SPH method.

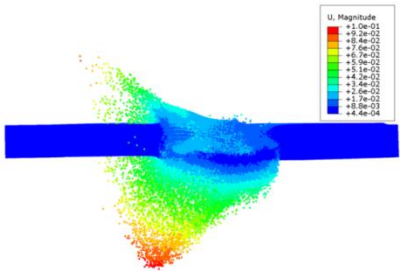

Fig. 16. Displacement value of cushion layer

5.3.3. Effect of rockfall shape on contact area

The summary discusses how the contact area between rockfall and cushion layer is affected by the shape factor and impact angle (Fig. 17). The impact force rises as the contact area increases while maintaining the same shape factor and varying impact angles. Note that when the spherical rockfall reached the maximum contact area, the maximum value lasted 0.5 ms. Therefore, when the soil was compressed to the ultimate depth , the rockfall remained stationary for a short period of time before rebounding occurred.

6. CONCLUSIONS

1. The corresponding errors of force and cushion layer deformation in numerical simulation and test are within 5.0 %, which verifies the accuracy of the SPH-FEM coupling algorithm. Under the same rockfall pattern, the peak force of rockfall decreases with the contact pose angle increasing, and the corresponding peak impact forces are 99 kN, 82.1 kN, and 73.0 kN with a shape factor of 0.79 and impact angle of 0°, 45° and 90°.
2. In the case of the same volume of rockfall, both the impact force and the impulse amplification factor decrease as the impact angle increases, and the smaller the shape factor of the rockfall, the more obvious the change. Taking the shape factor of 0.4 and the impact pose angle of 0° and 90° as examples, the peak impact force is amplified by 1.42 and 0.46 times, and the impulse is amplified by 1.0 and 0.77 times compared with that of the spherical rockfall.
3. In practical engineering calculations, the simplified method of calculating the impact response of rockfall by assuming they are spherical does not take into account how the shape and orientation of the rockfalls can affect the reliability of the structural design. Adopting the simplified method of rockfall shape in this paper helps to improve the existing theory of protective structure design. In addition, The SPH-FEM coupling method reasonably reproduces the physical process of pit formation in sandy soils and effectively simulates the flow behaviour of soil particles under impact conditions.

Acknowledgments

The research was conducted with assistance from the Foundation of Shandong Province Natural Science Foundation Youth Branch (ZR2021QE209).

REFERENCES

1. **Yan, P., Zhang, J., Fang, Q., Zhang, Y.** Numerical Simulation of the Effects of Falling Rock's Shape and Impact Pose on Impact Force and Response of RC Slabs *Construction and Building Materials* 160 2018: pp. 497 – 504. https://doi.org/10.1016/j.conbuildmat.2017.11.087
2. **Lari, S., Frattini, P., Crosta, G.B.** A Probabilistic Approach for Landslide Hazard Analysis *Engineering Geology* 182 2014: pp. 3 – 14. https://doi.org/10.1016/j.enggeo.2014.07.015
3. **Yang, X., Zhang, G., Yu, Y., Yu, Q., Lei, M., Ding, B.** Factors Influencing the Coefficient of Restitution in Rockfall Impacts *Natural Hazards Review* 22 (3) 2021: p. 04021024. https://doi.org/10.1061/(ASCE)NH.1527-6996.00004
4. **Ji, Z.M., Chen, Z.J., Niu, Q.H., Wang, T.H., Wang, T.J., Chen, T.L.** A Calculation Model of the Normal Coefficient of Restitution Based on Multi-factor Interaction Experiments *Landslides* 18 (4) 2021: pp. 1531 – 1553. https://doi.org/10.1007/s10346-020-01556-7
5. **Gentilini, C., Govoni, L., De Miranda, S., Gottardi, G., Ubertini, F.** Three-dimensional Numerical Modelling of Falling Rock Protection Barriers *Computers and Geotechnics* 44 2012: pp. 58 – 72. https://doi.org/10.1016/j.compgeo.2012.03.011
6. **Jin, Y., Yu, Z., Luo, L., Zhang, L., Xu, H., Qi, .** A Study on Energy Dissipation Mechanism of a Guided Flexible Protection System Under Rockfall Impact *Journal of Vibration and Shock* 40 (20) 2021: pp. 177 – 185+192. (in

Chinese)

7. **Chen, T.** A Study of the Distribution Ratio for Combined Spore–anchor Supporting of Unstable Rocks Based on FLAC 3D *Hydrogeology and Engineering Geology* 46 (01) 2019: pp. 64 – 70. (in Chinese)
8. **Chen, H., Zhou, Y., Tang, H.** Dynamic Stability Calculation Method for Unstable Sliding Rock Under Excavation Blasting Based on Time History Analysis *Journal of Vibration and Shock* 33 (5) 2014: pp. 31 – 34. (in Chinese)
9. **Ashwood, W., Hungr, O.** Estimating Total Resisting Force in Flexible Barrier Impacted by a Granular Avalanche Using Physical and Numerical Modeling *Canadian Geotechnical Journal* 53 (10) 2016: pp. 1700 – 1717. https://doi.org/10.1139/cgj-2015-0481
10. **Liu, C., Yu, Z., Zhao, S.** Quantifying the Impact of a Debris Avalanche Against a Flexible Barrier by Coupled DEM–FEM Analyses *Landslides* 17 (1) 2020: pp. 33 – 47. https://doi.org/10.1007/s10346-019-01267-8
11. **Escallón, J.P., Wendeler, C., Chatzi, E., Bartelt, P.** Parameter Identification of Rockfall Protection Barrier Components Through an Inverse Formulation *Engineering Structures* 77 2014: pp. 1 – 16. https://doi.org/10.1016/j.engstruct.2014.07.019
12. **Mougin, J.P., Perrotin, P., Mommessin, M., Tonnelo, J., Agbossou, A.** Rock Fall Impact on Reinforced Concrete Slab: an Experimental Approach *International Journal of Impact Engineering* 31 (2) 2005: pp. 169 – 183. https://doi.org/10.1016/j.ijimpeng.2003.11.005.
13. **Kishi, N., Konno, H., Ikeda, K., Matsuoka, K.G.** Prototype Impact Tests on Ultimate Impact Resistance of PC Rock-sheds *International Journal of Impact Engineering* 27 (9) 2002: pp. 969 – 985. https://doi.org/10.1016/S0734-743X(02)00019-2
14. **Delhomme, F., Mommessin, M., Mougin, J.P., Perrotin, P.** Behavior of a Structurally Dissipating Rock–shed: Experimental Analysis and Study of Punching Effects *International Journal of Solids and Structures* 42 (14) 2005: pp. 4204 – 4219. https://doi.org/10.1016/j.ijsolstr.2004.12.008
15. **Zhao, D.B., Yi, W.J., Kunnath, S.K.** Numerical Simulation and Shear Resistance of Reinforced Concrete Beams Under Impact *Engineering Structures* 166 2018: pp. 387 – 401.
16. **Calvetti, F., Prisco, C.D.** Rockfall Impacts on Sheltering Tunnels: Real-scale Experiments *Géotechnique* 62 (10) 2012: pp. 865 – 876. https://doi.org/10.1680/geot.9.P.036
17. **Lambert, S., Gotteland, P., Nicot, F.** Experimental Study of the Impact Response of Geocells as Components of Rockfall Protection Embankments *Natural Hazards and Earth System Sciences* 9 (02) 2009: pp. 459 – 467. https://doi.org/10.5194/nhess-9-459-2009
18. **Hennebert, P., Lambert, S., Fouillen, F., Charrasse, B.** Assessing the Environmental Impact of Shredded Tires as Embankment Fill Material *Canadian Geotechnical Journal* 51 (5) 2014: pp. 469 – 478. https://doi.org/10.1139/cgj-2013-0194
19. **Bertrand, D., Nicot, F., Gotteland, P., Lambert, S.** Modelling a Geo-composite Cell using Discrete Analysis *Computers and Geotechnics* 32 (8) 2005: pp. 564 – 577. https://doi.org/10.1016/j.compgeo.2005.11.004
20. **Plassiard, J.P., Donzé, F.V.** Optimizing the Design of Rockfall Embankments with a Discrete Element Method *Engineering Structures* 32 (11) 2010: pp. 3817 – 3826. https://doi.org/10.1016/j.engstruct.2010.08.025
21. **Ye, Y., Zeng, Y., Chen, X., Sun, H., Ma, W., Peng, Z.** Development of a Viscoelastoplastic Contact Model for the Size–and Velocity–dependent Normal Restitution Coefficient of a Rock Sphere Upon Impact *Computers and Geotechnics* 132 2021: p. 104014. https://doi.org/10.1016/j.compgeo.2021.104014
22. **Ronco, C., Oggeri, C., Peila, D.** Design of Reinforced Ground Embankments Used for Rockfall Protection *Natural Hazards and Earth System Sciences* 9 (4) 2009: pp. 1189 – 1199. https://doi.org/10.5194/nhess-9-1189-2009
23. **Labiouse, V., Descoeudres, F., Montani, S.** Experimental Study of Rock Sheds Impacted by Rock Blocks *Structural Engineering International* 6 (3) 1996: pp. 171 – 176. https://doi.org/10.2749/101686696780495536
24. **Yu, B., Yi, W., Zhao, H.** Experimental Study on the Maximum Impact Force by Rock Fall *Landslides* 15 (2) 2018: pp. 233 – 242. https://doi.org/10.1007/s10346-017-0876-x
25. **Delhomme, F., Mommessin, M., Mougin, J.P., Perrotin, P.** Simulation of a Block Impacting a Reinforced Concrete Slab with a Finite Element Model and a Mass-spring System *Engineering Structures* 29 (11) 2007: pp. 2844 – 2852. https://doi.org/10.1016/j.engstruct.2007.01.017
26. **Ji, Z.M., Hu, S.M., Chen, Z.J., Niu, Q.H., Wang, T.H., Wu, F.Q.** Laboratory Investigation of the Effect of the Rotational Speed on the Coefficient of Restitution *Engineering Geology* 292 2021: p. 106196. https://doi.org/10.1016/j.enggeo.2021.106196
27. **Mei, X., Hu, X., Luo, G., Du, Y., Ma, H., Wu, J.** Study on Recovery Coefficient and Peak Impact Force of Rockfall Impact Based on Elastic–plastic Theory *Journal of Vibration and Shock* 38 (8) 2019: pp. 14 – 20. (in Chinese)
28. **Perera, S., Lam, N., Pathirana, M., Zhang, L., Ruan, D., Gad, E.** Deterministic Solutions for Contact Force Generated by Impact of Windborne Debris *International Journal of Impact Engineering* 91 2016: pp. 126 – 141. https://doi.org/10.1016/j.ijimpeng.2016.01.002
29. **Huang, R., Liu, W.** In–situ Test Study of Characteristics of Rolling Rock Blocks Based on Orthogonal Design *Chinese Journal of Rock Mechanics and Engineering* 28 (5) 2009: pp. 882 – 891. (in Chinese)
30. **Yan, P., Fang, Q., Zhang, J., Zhang, Y., Chen, L., Fan, Y.** Experimental Study of Different Typical Shape Falling-rocks Impacting on the Sand Cushion and Dimensionless Analysis *Explosion and Shock Waves* 41 (7) 2021: pp. 96 – 111. (in Chinese)
31. **Pichler, B., Hellmich, C., Mang, H.A.** Impact of Rocks onto Gravel Design and Evaluation of Experiments *International Journal of Impact Engineering* 31 (5) 2005: pp. 559 – 578. https://doi.org/10.1016/j.ijimpeng.2004.01.007
32. **Peila, D., Oggeri, C., Castiglia, C.** Ground Reinforced Embankments for Rockfall Protection: Design and Evaluation of Full Scale Tests *Landslides* 4 (3) 2007: pp. 255 – 265. https://doi.org/10.1007/s10346-007-0081-4
33. **Yang, H., Zhou, X.** A New Approach to Calculate Trajectory of Rockfall *Rock and Soil Mechanics* 30 (11) 2009: pp. 3411 – 3416. (in Chinese)
34. **Wang, B., Cavers, D.S.** A Simplified Approach for Rockfall Ground Penetration and Impact Stress Calculations *Landslides* 5 (3) 2008: pp. 305 – 310. https://doi.org/10.1007/s10346-008-0123-6
35. **Dattola, G., Crosta, G.B., Di Prisco, C.** Investigating the Influence of Block Rotation and Shape on the Impact Process

International Journal of Rock Mechanics and Mining Sciences 147 2021: p. 104867. https://doi.org/10.1016/j.ijrmms.2021.104867

36. **Di Prisco, C., Vecchiotti, M.** Design Charts for Evaluating Impact Forces on Dissipative Granular Soil Cushions *Journal of Geotechnical and Geoenvironmental Engineering* 136 (11) 2010: pp. 1529 – 1541. https://doi.org/10.1061/(ASCE)GT.1943-5606.0000363
37. **Zhang, Y., He, B., Xie, L., Zhao, P.** Test Results and Analysis of Rockfall Impact Sand Cushion with Different Shapes *Science Technology and Engineering* 22 (32) 2022: pp. 14347 – 14352. (in Chinese)
38. **Zeng, Q., Yang, Y., Zhang, X., Wan, L., Zhou, J., Yin, G.** Study on Metal Plate Vibration Response Under Coal-gangue Impact Based on 3D Simulation *Arabian Journal for Science and Engineering* 44 (9) 2019: pp. 7567 – 7580. https://doi.org/10.1007/s13369-019-03853-3
39. **Wang, X., Xia, Y., Zhou, T.** Theoretical Analysis of Rockfall Impacts on the Soil Cushion Layer of Protective Structures *Advances in Civil Engineering* 2018: pp. 1 – 18. https://doi.org/10.1155/2018/9324956.
40. **Chen, C., Liu, C., Chen, L., Zhao, S.** Study on Impact Force of Rock–fall onto Rock Shed Tunnel *Journal of Highway and Transportation Research and Development* 32 (01) 2015: pp. 102 – 109. (in Chinese)
41. **Luo, J., Xiao, J., Ma, K., Mao, J.** SPH–FEM Coupled Method for Analyzing a Hemispherical Shell Impact Soil *Journal of Vibration and Shock* 36 (17) 2017: pp. 195 – 199+230. (in Chinese)
42. **Shen, W., Zhao, T., Dai, F., Jiang, M., Zhou, G.D.** DEM Analyses of Rock Block Shape Effect on the Response of Rockfall Impact Against a Soil Buffering Layer *Engineering Geology* 249 2019: pp. 60 – 70. https://doi.org/10.1016/j.enggeo.2018.12.011
43. **Liu, C., Yu, Z., Zhao, S.** Consideration of Maximum Impact Force Design for a Rock Shed Against Dry Granular Flow *European Journal of Environmental and Civil Engineering* 26 (7) 2022: pp. 2963 – 2984. https://doi.org/10.1080/19648189.2020.1779135
44. **Johnson, G.R., Stryk, R.A.** Conversion of 3D Distorted Elements into Meshless Particles During Dynamic Deformation *International Journal of Impact Engineering* 28 (9) 2003: pp. 947 – 966. https://doi.org/10.1016/S0734-743X(03)00012-5
45. **Liu, C., Yu, Z.,Guo, L., Zhao, S.** Numerical Simulation for Rock–fall Impacting an Arch RC Hangar Tunnel Based on SPH–FEM Coupled Method *Journal of Vibration and Shock* 38 (13) 2019: pp. 118 – 125. (in Chinese)
46. **Lubliner, J., Oliver, J., Oller, S., Oñate, E.** A Plastic–damage Model for Concrete *International Journal of Solids and Structures* 25 (3) 1989: pp. 299 – 326. https://doi.org/10.1016/0020-7683(89)90050-4
47. **Wang, Z., Yu, Z.** Concrete Damage Model Based on Energy Loss *Journal of Building Materials* 25 (3) 1989: pp. 299 – 326. (in Chinese)
48. **Yuan, J., Huang, R., Pei, X.** Test Research on Rockfall Impact Force *Rock and Soil Mechanics* 35 (01) 2014: pp. 48 – 54. (in Chinese)